

Optical Spectra and Localization of Excitons in Inhomogeneous Helical Cylindrical Aggregates

Cătălin Didraga and Jasper Knoester*

*Institute for Theoretical Physics and Materials Science Centre,
University of Groningen, Nijenborgh 4, 9747 AG Groningen, The Netherlands*

(Dated: June 14, 2018)

We study the linear optical properties of helical cylindrical molecular aggregates accounting for the effects of static diagonal disorder. Absorption, linear dichroism, and circular dichroism spectra are presented, calculated using brute force numerical simulations and a modified version of the coherent potential approximation that accounts for finite size effects. Excellent agreement between both approaches is found. It is also shown that the inclusion of disorder results in a better agreement between calculated and measured spectra for the chlorosomes of green bacteria as compared to our previous report, where we restricted ourselves to homogeneous cylinders [J. Phys. Chem. B **106**, 11474 (2002)]. We also investigate the localization properties of the excitons responsible for the optical response. By analyzing an autocorrelation function of the exciton wave function, we find a strongly anisotropic localization behavior, closely following the properties of chiral wave functions which previously have been found for homogeneous helical cylinders [J. Chem. Phys. **121**, 946 (2004)]. It is shown that the circular dichroism spectrum may still show a strong dependence on the cylinder length, even when the exciton wave function is localized in a region small compared to the cylinder's size.

PACS numbers: 71.35.Aa; 78.30.Ly; 71.35.Cc 78.67.-n

I. INTRODUCTION

The optical properties and optical dynamics of molecular aggregates with a cylindrical geometry currently draw considerable attention. Both natural and synthetic forms of such molecular nanotubes are investigated. Among the natural systems, the rod shaped light-harvesting complexes in the chlorosomes of green bacteria are well-known examples.¹ The chlorosomes of *Chloroflexus aurantiacus* contain tens of thousands of bacteriochlorophyll molecules self-assembled in cylindrical structures with a monolayer wall of roughly 5 nm diameter and a length of hundreds of nanometers.^{2,3,4,5} The light-harvesting system of the bacterium *Chlorobium tepidum* also contains cylindrical aggregates, with a bilayer wall and a diameter of roughly 10 nm.⁶ These natural systems should be referred to as J aggregates, as the absorption spectrum is red-shifted relative to the transition frequency of a single bacteriochlorophyll molecule.

J aggregates with a cylindrical geometry have recently also been prepared via synthetic routes. In particular a class of substituted 5,5',6,6'-tetrachlorobenzimidacarbocyanine dyes has been created that forms such aggregates; the cylindrical geometry was revealed using cryo-TEM.^{7,8} It has been demonstrated that the precise morphology as well as the details of the optical properties depends on the nature of the substituents and the solvent.^{9,10} These synthetic cylinders usually have bilayer walls with an

outer diameter of about 15 nm and a wall thickness of 4 nm. The cylinder length extends to several hundreds of nanometers. Recently, the (helical) arrangement of the molecules inside the bilayer wall of such aggregates has been determined for the first time. This was done for the aggregates of the dye 3,3'-bis(3-sulfopropyl)-5,5',6,6'-tetrachloro-1,1'-dioctylbenzimidacarbocyanine (C8S3), by modeling the data from cryo-TEM, absorption and linear dichroism measurements.¹⁰ A Frenkel exciton model based on two weakly interacting bricklayer monolayers wrapped on cylindrical surfaces of appropriate diameter gave a good fit to experiment. Very recently, it has been discovered that bilayer molecular nanotubes (diameter 14 nm) may also be formed through self-assembly of amphiphilic hexi-*peri*-hexabenzocoronene molecules.¹¹ Another class of synthetic cylindrical aggregates are those formed through self-assembly of the dye meso-tetra(4-sulfonatophenyl)porphyrin (TTPS₄) in acidic aqueous solution.^{12,13} From small angle x-ray scattering (SAXS)¹² and atomic force microscopy (AFM)¹³ it has been concluded that these aggregates are hollow monolayer tubes with a diameter of about 20 nm. Finally, it has been shown that under the influence of tetrahedral chemical defects conjugated polymers may also adopt ordered cylindrical conformations.¹⁴

In previous model studies of cylindrical aggregates, we have mainly restricted ourselves to homogeneous aggregates, i.e., we have ignored the role of disorder on the Frenkel exciton states that determine the optical response.^{15,16,17,18} An important simplification occurs in this case, as the cylindrical symmetry may then be used to distinguish excitons in classes (bands) of different transverse quantum number k_2 , which describes the Bloch nature of the exciton wave function in the direc-

*Corresponding author. Fax: 31-50-3634947. E-mail: knoester@phys.rug.nl

tion along the circumference of the cylinder.¹⁷ The exciton eigenstates may then be determined from a set of one-dimensional effective Hamiltonians for each value of k_2 . Importantly, the introduction of the transverse quantum number dictates simple selection rules, which state that only states with $k_2 = 0$ or $k_2 = \pm 1$ can be observed in linear optics. States in the $k_2 = 0$ band give rise to absorption polarized along the cylinder's axis, while states with $k_2 = \pm 1$ yield a polarization perpendicular to this axis. For each of these three bands only a few strongly allowed (superradiant) exciton states occur.^{17,18}

In spite of the fact that usually appreciable energetic or interaction disorder occur in self-assembled molecular aggregates, it turns out that a homogeneous aggregate model, with the simple selection rules discussed above, does describe the salient features of experimentally observed spectra. For instance, using this model, the experimentally observed variation in the CD spectra of the chlorosomes of *Chloroflexus aurantiacus* was explained.¹⁷ Similarly, the polarization dependent spectra of the bilayer C8S3 cylinders are rather well described neglecting the role of disorder.¹⁰ We have shown, however, that the inclusion of static energy disorder does improve the comparison to experiment for the latter case.¹⁰ Similarly, model results for chlorosomes that do account for disorder also show a better quantitative comparison to experiment.¹⁹

The aim of this paper is to systematically study the effect of static diagonal disorder on the optical spectra of cylindrical molecular aggregates and to study the exciton localization properties caused by the presence of disorder. While the formalism used applies to general cylindrical aggregates, we will in explicit calculations restrict ourselves to cylinders of the structure of chlorosomes of *Chloroflexus aurantiacus*. As observable quantities, we will focus on the absorption, linear dichroism (LD), and circular dichroism (CD) spectra. The disorder averages of these spectra are calculated using numerical simulations as well as a modified version of the coherent potential approximation (CPA) that accounts for finite-size effects.

Localization properties have been extensively studied for Frenkel excitons in linear^{20,21,22,23} and circular^{24,25,26} aggregates. For the higher dimensional cylindrical aggregates, such studies have not been performed yet. We will fill this gap by investigating the inverse participation ratio and an autocorrelation function of the wave function. Using the latter, we will show a strong anisotropy in the localization properties of the excitons, which may be traced back to the recently discovered chiral behavior of the exciton wave functions on finite homogeneous cylindrical aggregates,¹⁸ dictated by the behavior of the dipolar excitation exchange interactions in the system. We will also demonstrate that the CD spectrum may exhibit a dependence on the cylinder's length, even when the excitons are localized on regions small compared to the its size.

The outline of this paper is as follows. In Sec. II we will present the exciton model and give the general expres-

sions for the quantities of interest, in particular for the spectra and the localization characteristics. Section III is dedicated to explain the modified version of the CPA. Results for the spectra are presented and discussed in Sec. IV, while in Sec. V we do the same for the localization characteristics. Finally, we present our conclusions in Sec. VI.

II. MODEL AND QUANTITIES OF INTEREST

a. Aggregate structure, Hamiltonian, and eigenstates.

For the structure of the cylindrical aggregate we will use the same model and notation as described in Ref. 17 and depicted in Figure 1. The aggregate consists of a stack of N_1 rings of radius R (labeled $n_1 = 1, \dots, N_1$), each containing N_2 molecules. The distance between neighboring rings is denoted h . Neighboring rings are rotated relative to each other over a helical angle γ , with $0 \leq \gamma < 2\pi/N_2$. Connecting the closest molecules on neighboring rings, one observes that the aggregate may be viewed as N_2 helices each containing N_1 molecules, winding around the cylinder (the dashed line in Figure 1 indicates one such helix). Each molecule may now be labeled $\mathbf{n} = (n_1, n_2)$, where n_1 denotes the ring on which the molecule resides, while n_2 denotes the helix on which it lies. The total number of molecules in the aggregate is denoted $N = N_1 N_2$. In Ref. 17 we explained the general nature of this structural model.

All molecules are modeled as identical two-level systems, with transition dipoles $\boldsymbol{\mu}_{\mathbf{n}}$ that are equal in magnitude (μ) and have equal orientations relative to the frame of the cylinder at the position of the molecule. In particular, all molecular dipoles make an angle β with the cylinder axis (referred to as the z axis), while the projection of each dipole on the xy -plane makes an angle α with the local tangent to the rings. Explicitly, the x , y , and z components of the molecular position vectors and dipole moments are given by the three-dimensional vectors:

$$\mathbf{r}_{\mathbf{n}} = (R \cos(n_2 \phi_2 + n_1 \gamma), R \sin(n_2 \phi_2 + n_1 \gamma), n_1 h) \quad (1)$$

and

$$\boldsymbol{\mu}_{\mathbf{n}} = (-\mu \sin \beta \sin(n_2 \phi_2 + n_1 \gamma - \alpha), \mu \sin \beta \cos(n_2 \phi_2 + n_1 \gamma - \alpha), \mu \cos \beta), \quad (2)$$

respectively, with $\phi_2 = 2\pi/N_2$.

The electronically excited states of the aggregate are described by the Frenkel exciton Hamiltonian with static diagonal disorder. Setting $\hbar = 1$, we have

$$H = \sum_{\mathbf{n}} (\omega_0 + \epsilon_{\mathbf{n}}) b_{\mathbf{n}}^\dagger b_{\mathbf{n}} + \sum'_{\mathbf{n}, \mathbf{m}} J(\mathbf{n} - \mathbf{m}) b_{\mathbf{n}}^\dagger b_{\mathbf{m}}, \quad (3)$$

where $b_{\mathbf{n}}^\dagger$ and $b_{\mathbf{n}}$ denote the Pauli operators for creation and annihilation of an excitation on molecule \mathbf{n} , respectively.^{27,28,29,30} Furthermore, ω_0 is the average

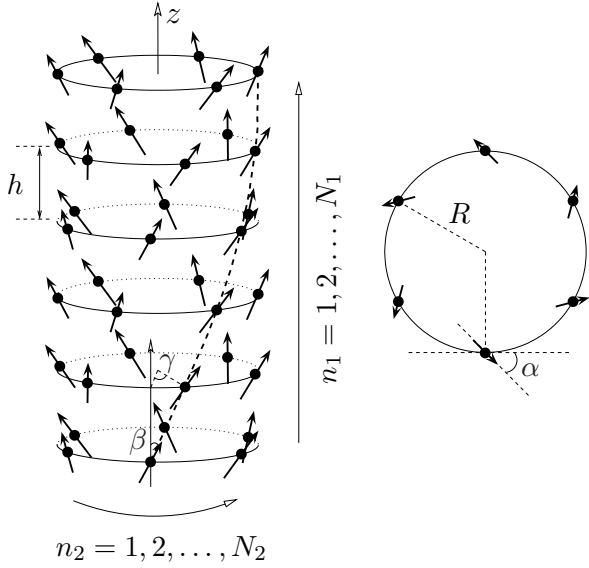


FIG. 1: Cylindrical aggregate consisting of a stack of N_1 rings, labeled $n_1 = 1, 2, \dots, N_1$, that each contain N_2 molecules, labeled $n_2 = 1, 2, \dots, N_2$. The arrows indicate the transition dipoles, which are equal in magnitude (μ) and make an angle β with the cylinder axis. The projection of each dipole on the plane of the rings makes an angle α with the local tangent to the ring (see projection of one ring displayed to the right). Each ring is rotated with respect to the previous one over an angle γ , so that we may view the aggregate as a collection of N_2 parallel helices on the cylinder's surface. One such helix is indicated by the dashed curve. The label n_2 in fact labels the helices.

molecular transition frequency and $\epsilon_{\mathbf{n}}$ is the static random energy offset at site \mathbf{n} , induced by slow solvent effects. $J(\mathbf{n} - \mathbf{m})$ is the excitation transfer interaction between molecules \mathbf{n} and \mathbf{m} . Due to the symmetry of the system the interaction only depends on the relative positions of the two molecules. The prime on the summation indicates that the term with $\mathbf{n} = \mathbf{m}$ is excluded from the summation. We assume that $J(\mathbf{n} - \mathbf{m})$ results from dipole-dipole interactions, giving it the explicit form

$$J(\mathbf{n} - \mathbf{m}) = \frac{\boldsymbol{\mu}_{\mathbf{n}} \cdot \boldsymbol{\mu}_{\mathbf{m}}}{|\mathbf{r}_{\mathbf{nm}}|^3} - 3 \frac{(\boldsymbol{\mu}_{\mathbf{n}} \cdot \mathbf{r}_{\mathbf{nm}})(\boldsymbol{\mu}_{\mathbf{m}} \cdot \mathbf{r}_{\mathbf{nm}})}{|\mathbf{r}_{\mathbf{nm}}|^5}, \quad (4)$$

with $\mathbf{r}_{\mathbf{nm}} = \mathbf{r}_{\mathbf{n}} - \mathbf{r}_{\mathbf{m}}$.

The Hamiltonian Eq. (3) differs from the one discussed in Ref. 17 only in the inclusion of random energy offsets $\epsilon_{\mathbf{n}}$. We will assume that the energy offsets on different molecules are uncorrelated and follow a Gaussian distribution $\mathcal{P}(\epsilon_{\mathbf{n}})$ with standard deviation σ . Hence, each $\epsilon_{\mathbf{n}}$ is taken independently from the distribution

$$\mathcal{P}(\epsilon_{\mathbf{n}}) = \frac{1}{\sqrt{2\pi}\sigma} \exp\left(-\frac{\epsilon_{\mathbf{n}}^2}{2\sigma^2}\right). \quad (5)$$

To describe the linear optical response of the aggregate, it suffices to consider the space of one-exciton states, i.e., those states in which the molecules of the cylinder share

one excitation. The general form of these eigenstates reads

$$|q\rangle = \sum_{\mathbf{n}} \varphi_q(\mathbf{n}) b_{\mathbf{n}}^\dagger |g\rangle, \quad (6)$$

where $|g\rangle$ denotes the overall ground state, in which all molecules are in their ground state. We have used the label q to distinguish the N one-exciton states; the quantity $\varphi_q(\mathbf{n})$ denotes the amplitude of the q th state on molecule \mathbf{n} . These amplitudes are obtained by diagonalizing the $N \times N$ one-exciton Hamiltonian, which has the quantities $\omega_0 + \epsilon_{\mathbf{n}}$ as diagonal elements and the $J(\mathbf{n} - \mathbf{m})$ as off-diagonal ones. The eigenvectors $\varphi_q(\mathbf{n})$ will be assumed to be normalized to unity. Unless stated otherwise, we will impose open boundary conditions along the z axis.

In the absence of disorder ($\sigma = 0$), the label q may be replaced by a two-dimensional label $\mathbf{k} = (k_1, k_2)$, where k_2 denotes the wave number describing the Bloch momentum of the exciton state along the ring direction, while k_1 labels the N_1 possible exciton states in each of the N_2 different bands characterized by one value of k_2 .^{17,18} The diagonalization then separates into N_2 independent effective one-dimensional problems. In the current general case of disorder, we cannot make this decomposition of the quantum labels, and we will keep the general label q . We note that with the breakdown of the separation into transverse (k_2) and longitudinal (k_1) quantum numbers, also the strict distinction between states polarized parallel ($k_2 = 0$) and perpendicular ($k_2 = \pm 1$) to the z axis breaks down. In general, the dipoles of the exciton states in disordered cylinders may have any orientation relative to the z axis.

b. Optical spectra. We will be interested in calculating the absorption, LD, and CD spectra in the presence of diagonal disorder. The general expressions for these spectra in terms of the one-exciton energies E_q and eigenvector components $\varphi_q(\mathbf{n})$ follow from linear response theory and take the generic form¹⁷

$$S(\omega) = \left\langle \sum_q X_q \delta(\omega - E_q) \right\rangle, \quad (7)$$

with strength

$$X_q = \sum_{\mathbf{n}, \mathbf{m}} \varphi_q(\mathbf{n}) \varphi_q^*(\mathbf{m}) X_{\mathbf{n}, \mathbf{m}}. \quad (8)$$

Here, $S(\omega)$ stands for $A(\omega)$, $LD(\omega)$, and $CD(\omega)$ in case of the absorption, LD, and CD spectrum, respectively, and the angular brackets $\langle \dots \rangle$ denote the average over the random energy offsets. Furthermore, the quantities $X_{\mathbf{n}, \mathbf{m}}$ are the corresponding strengths in the site representation, which take the form

$$X_{\mathbf{n}, \mathbf{m}}^A = \frac{1}{3} \mu^2 \cos^2 \beta + \frac{1}{3} \mu^2 \cos \xi \sin^2 \beta, \quad (9)$$

$$X_{\mathbf{n}, \mathbf{m}}^{LD} = \mu^2 \cos^2 \beta - \frac{1}{2} \mu^2 \cos \xi \sin^2 \beta, \quad (10)$$

and

$$X_{\mathbf{n},\mathbf{m}}^{CD} = \frac{\pi\mu^2}{6\lambda} [R(1 - \cos \xi) \sin(2\beta) \cos \alpha - (n_1 - m_1)h \sin \xi \sin^2 \beta] . \quad (11)$$

for the three spectra considered. Here, $\xi \equiv [(n_2 - m_2)\phi_2 + (n_1 - m_1)\gamma]$ and λ denotes the wavelength of the light. In the above expressions for the absorption and CD spectra, an isotropic average over orientations of the cylinder has been used (appropriate for an isotropic solution), while in case of the LD spectrum, a uniform average over angles of rotation around the cylinder's axis was inferred (appropriate for samples with perfect alignment of the cylinders). Any (unlikely) correlation between orientation and disorder realization has been neglected. For future reference it is useful to note that also the density of states, $\rho(\omega)$, follows the generic expression Eq. (7), with $X_{\mathbf{n},\mathbf{m}}^\rho = \delta_{\mathbf{n},\mathbf{m}}$, implying $X_q^\rho = 1$.

The disorder averaged spectra and density of states in principle may be calculated using straightforward numerical simulations, in which one generates a number of random disorder realizations $\{\epsilon_{\mathbf{n}}\}$ and for each realization performs an explicit diagonalization of the one-exciton Hamiltonian to obtain the quantities E_q and $\varphi_q(\mathbf{n})$. For one-dimensional (linear or circular) molecular aggregates this is common practice. For higher-dimensional aggregates, however, such as planes or cylinders, this method may be quite demanding, due to the large number of molecules involved in these systems and the tendency for the collective excitations to be more delocalized in higher dimensions. This motivates the use of alternative, albeit approximate, methods to calculate the average spectra. A well-known example is the coherent potential approximation (CPA),^{31,32} which previously has been applied with success to calculate spectra of, for instance, isotopically mixed aromatic crystals (dichotomic disorder),^{33,34} one-component systems with Gaussian diagonal disorder,^{35,36} and two-component systems with bi-Gaussian diagonal disorder.³⁷

In this paper, we will use both brute-force numerical simulations and the CPA to calculate the spectra and the density of states. We will extend the usual CPA to account for finite-size effects (Section III) and show that this modified CPA gives excellent agreement with numerical simulations, in fact significantly better than its conventional implementation.

c. Localization characteristics. As is well known, the presence of diagonal disorder leads to the localization of the excitonic eigenstates.³⁸ In order to have quantitative information on this localization, we will analyze the inverse participation ratio and an autocorrelation function of the wave function. Both quantities can only be addressed within a numerical simulation. The energy dependent inverse participation ratio is defined through^{20,21,22,39}

$$\mathcal{L}(\omega) = \left\langle \sum_q \left[\sum_{\mathbf{n}} |\varphi_q(\mathbf{n})|^4 \delta(\omega - E_q) \right] \right\rangle / \rho(\omega) . \quad (12)$$

The participation ratio, \mathcal{L}^{-1} , is generally accepted as a typical value for the number of molecules participating in the eigenstates at energy ω . For example, a state localized on a single molecule has $\mathcal{L}(\omega) = 1$, whereas for the completely delocalized states on a homogeneous cylinder $\mathcal{L}(\omega) \sim 1/N$. In the latter case, the precise value depends on the boundary conditions and on the possible combination of degenerate complex eigenstates to real ones. If we use periodic boundary conditions along the z axis and use real sin and cos forms for the transverse and longitudinal Bloch wave functions, all states (except a few⁴⁰) have a participation ratio $9/(4N)$. For the same boundary conditions using complex wave functions, all states have $\mathcal{L}(\omega) = 1/N$. If we use open boundary conditions with real transverse wave functions and accept the ansatz solutions for the longitudinal wave functions analyzed in Ref. 18, we obtain (again with a few exceptions) the value $9/[4(N_1 + 1)N_2] \approx 9/(4N)$.

Alternative measures for the extent of the exciton wave function have also been considered, for instance, autocorrelation functions of the wave function were used to study the ring-shaped LH2 antenna system.^{24,41} Correlation functions are particularly useful when dealing with anisotropic higher-dimensional systems, such as cylindrical aggregates, as they allow for a study of the localization properties along different spatial directions. Such information cannot be extracted from the inverse participation ratio. Hence, we define the autocorrelation function

$$\mathcal{C}(\mathbf{n}; \omega) = \left\langle \sum_q \sum_{\mathbf{m}} |\varphi_q(\mathbf{m}) \varphi_q^*(\mathbf{m} + \mathbf{n})| \delta(\omega - E_q) \right\rangle / \rho(\omega), \quad (13)$$

where the summation over \mathbf{m} extends over $m_1 = 1, \dots, N_1 - n_1$ and $m_2 = 1, \dots, N_2$ in order to be consistent with open boundary conditions in the n_1 direction.

The generic form of $\mathcal{C}(\mathbf{n}; \omega)$ on the (n_1, n_2) plane is a structure that peaks at the origin $(0, 0)$ (where it has the value unity) and which (after averaging over a sufficient number of disorder realizations) has inversion symmetry with respect to the origin. The form of the peak shows in what direction the exciton wave functions at energy ω are most localized or extended. Finally, from the autocorrelation one can define a localization measure (alternative to $\mathcal{L}^{-1}(\omega)$) for the total number of molecules participating in the typical wave function at energy ω . We will denote this measure by $N_{del}^C(\omega)$ and define it as the total number of \mathbf{n} values (molecules) with $\mathcal{C}(\mathbf{n}; \omega) > \mathcal{C}(\mathbf{0}; \omega)/e = 1/e$ (e the base of the natural logarithm). It should be stressed that both the participation ratio and $N_{del}^C(\omega)$ represent typical numbers and cannot be expected to give exactly the same result. However, one does expect these two measures to vary in a similar way with energy, disorder strength, or system size. We will come back to this in Sec. V.

III. MODIFIED COHERENT POTENTIAL APPROXIMATION

In this section, we address some essential technical aspects to use the CPA when calculating the optical spectra. The method as such is well-documented in text books,^{42,43} which is why we only focus on two aspects that are specific to our application. The first one concerns reducing the general expression Eq. (7) for the spectra to a form that can be addressed within the CPA. The second one concerns the treatment of finite systems, where periodic boundary conditions should be avoided.

The CPA is a method that yields an approximate form for the disorder averaged (retarded) Green's function $\langle \hat{G}(\omega) \rangle$, with

$$\hat{G}(\omega) = (\omega \hat{1} - H + i\eta)^{-1}. \quad (14)$$

Here, $\hat{1}$ is the unit operator, η is a positive infinitesimal constant, and H is the Hamiltonian Eq. (3). Using the Green's function, we may rewrite Eq. (7) for the spectra as

$$S(\omega) = -\frac{1}{\pi} \text{Im} \left\langle \sum_q X_q \langle q | \hat{G}(\omega) | q \rangle \right\rangle. \quad (15)$$

As the eigenstates $|q\rangle$ and the strengths X_q depend on the disorder realization, some care is needed to reduce Eq. (15) to a form that only contains $\langle \hat{G}(\omega) \rangle$.

We first use Eq. (8) for X_q in terms of $X_{\mathbf{n},\mathbf{m}}$. Realizing that $\varphi_q(\mathbf{n}) = \langle \mathbf{n} | q \rangle$ and using the fact that the $X_{\mathbf{n},\mathbf{m}}$ do not depend on the disorder realization [see Eqs. (9), (10), and (11)], we may rewrite

$$S(\omega) = -\frac{1}{\pi} \text{Im} \sum_{\mathbf{n},\mathbf{m}} X_{\mathbf{n},\mathbf{m}} \langle \mathbf{n} | \langle \hat{G}(\omega) \rangle | \mathbf{m} \rangle. \quad (16)$$

We now change to the basis of eigenstates of the system in the absence of disorder ($\sigma = 0$), in which case we replace the state label q by the two-dimensional label $\mathbf{k} = (k_1, k_2)$ (eigenvectors $\varphi_{\mathbf{k}}(\mathbf{n})$ and energies $E_{\mathbf{k}}$), as explained in Sec. II. The advantage to do this will become clear below. On this basis, Eq. (16) takes the form

$$S(\omega) = -\frac{1}{\pi} \text{Im} \sum_{\mathbf{k},\mathbf{k}'} X_{\mathbf{k},\mathbf{k}'} \langle \mathbf{k} | \langle \hat{G}(\omega) \rangle | \mathbf{k}' \rangle, \quad (17)$$

where we defined

$$X_{\mathbf{k},\mathbf{k}'} = \sum_{\mathbf{n},\mathbf{m}} X_{\mathbf{n},\mathbf{m}} \varphi_{\mathbf{k}}(\mathbf{n}) \varphi_{\mathbf{k}'}^*(\mathbf{m}). \quad (18)$$

We now take advantage of the fact that within the CPA the averaged Green's function $\langle \hat{G}(\omega) \rangle$ is replaced by the Green's function of the same system in the absence of disorder, but with an ω dependent and \mathbf{k} independent complex self-energy $\Sigma(\omega)$ added to the exciton energies

$E_{\mathbf{k}}$. Thus, within the CPA $\langle \hat{G}(\omega) \rangle$ is by definition diagonal in the \mathbf{k} basis. Hence,

$$\begin{aligned} S(\omega) &= -\frac{1}{\pi} \text{Im} \sum_{\mathbf{k}} X_{\mathbf{k},\mathbf{k}} \langle \mathbf{k} | \langle \hat{G}(\omega) \rangle | \mathbf{k} \rangle \\ &= -\frac{1}{\pi} \text{Im} \sum_{\mathbf{k}} X_{\mathbf{k},\mathbf{k}} \frac{1}{\omega - E_{\mathbf{k}} - \Sigma(\omega) + i\eta}. \end{aligned} \quad (19)$$

We proceed by using the Bloch nature of the eigenvectors $\varphi_{\mathbf{k}}(\mathbf{n})$ in the ring direction,

$$\varphi_{\mathbf{k}}(\mathbf{n}) = (N_2)^{-1/2} \exp[i2\pi k_2 n_2 / N_2] \varphi_{k_1}(n_1; k_2) \quad (20)$$

with the integer k_2 the transverse wave number and $\varphi_{k_1}(n_1; k_2)$ the longitudinal wave function.¹⁷ Then the strengths $X_{\mathbf{k},\mathbf{k}}^A$, $X_{\mathbf{k},\mathbf{k}}^{LD}$, and $X_{\mathbf{k},\mathbf{k}}^{CD}$ for the three spectra considered can be expressed in terms of the $\varphi_{k_1}(n_1; k_2)$. This algebra was already performed in Ref. 17, yielding the oscillator strength $O_{\mathbf{k}}$, the LD strength $L_{\mathbf{k}}$, and the rotational strength $R_{\mathbf{k}}$. Combining all these expressions, we recover for the final CPA results Eqs. (20), (24), and (31) of Ref. 17 for the absorption, the LD, and the CD spectrum, respectively, except that $\delta(\omega - E_{\mathbf{k}})$ in these expressions is replaced by $-\frac{1}{\pi} \text{Im}(\omega - E_{\mathbf{k}} - \Sigma(\omega) + i\eta)^{-1}$. In particular we find that, like in the homogeneous case, only terms with $k_2 = 0, \pm 1$ contribute to the three spectra, with the $k_2 = 0$ states having a transition dipole along the z axis and the other two (degenerate) bands having a dipole perpendicular to it. In contrast to the homogeneous case, however, to calculate the CPA spectra we still need the eigenenergies of all states in all k_2 bands. The reason is that these energies occur in the quantity $g_0(\omega)$ (Eq. (23)), which is needed to solve for the self-energy.

We finally mention that within the CPA, the density of states is simply given by Eq. (19) with $X_{\mathbf{k},\mathbf{k}}^p$ replaced by 1.

Since the numerical diagonalization of the N_2 effective one-dimensional problems that yield the longitudinal eigenfunctions $\varphi_{k_1}(n_1; k_2)$ and the energies $E_{\mathbf{k}}$ is straightforward, the only remaining problem is to determine the self-energy $\Sigma(\omega)$. Within the CPA, $\Sigma(\omega)$ obeys a self-consistency equation, derived by neglecting correlations between scattering events on different molecules. The resulting self-consistency equation reads^{42,43}

$$\left\langle \frac{\epsilon_{\mathbf{n}} - \Sigma(\omega)}{1 - (\epsilon_{\mathbf{n}} - \Sigma(\omega)) \langle \hat{G}(\omega) \rangle_{\mathbf{nn}}} \right\rangle = 0, \quad (21)$$

where the disorder average now is a simple integration over $\epsilon_{\mathbf{n}}$, weighted by the distribution $\mathcal{P}(\omega_{\mathbf{n}})$. The site diagonal element of the averaged Green's function is

$$\langle \hat{G}(\omega) \rangle_{\mathbf{nn}} = \sum_{\mathbf{k}} \frac{|\varphi_{\mathbf{k}}(\mathbf{n})|^2}{\omega - E_{\mathbf{k}} - \Sigma(\omega) + i\eta} \quad (22)$$

The CPA has been developed for large systems, where periodic boundary conditions can safely be applied to

obtain the homogeneous solutions. In that case we have $|\varphi_{\mathbf{k}}(\mathbf{n})|^2 = 1/N$, with N the total number of molecules in the system. Substituting this in Eq. (22), we observe that the diagonal element of the Green's function becomes site-independent, which in fact is necessary in order for the self-energy following from Eq. (21) to be site-independent. The latter fact is implicit in the CPA by assuming from the very beginning that the self-energy does not depend on \mathbf{k} . Conversely, if in Eq. (22) we would boldly substitute the solution for the homogeneous solution with open boundary conditions applied along the n_1 direction, we would obtain a site-dependent (n_1 dependent) self-energy, which would be inconsistent in the context of the CPA.

Yet, as we will be interested in studying the effect of the cylinder length on the spectra, we prefer not to use periodic boundary conditions in the n_1 direction. One way out of this impasse is to construct artificially a diagonal element of the Green's function which is site invariant. This can be done by approximating $\langle \hat{G}(\omega) \rangle_{\mathbf{nn}}$ by its mean

$$\begin{aligned} \langle \hat{G}(\omega) \rangle_{\mathbf{nn}} &\approx \frac{1}{N} \sum_{\mathbf{n}} \langle \hat{G}(\omega) \rangle_{\mathbf{nn}} \\ &= \frac{1}{N} \sum_{\mathbf{k}} \frac{1}{\omega - E_{\mathbf{k}} - \Sigma(\omega) + i\eta} \equiv g_0(\omega), \end{aligned} \quad (23)$$

which implies in particular that the local density of states is approximated by the normalized total one. We note that in spite of this approximation, the self-energy still contains information about the system's finite size, as the finite-size energies $E_{\mathbf{k}}$ will be used when evaluating $g_0(\omega)$. Moreover, when calculating the spectra and density of states (Eq. (19) with the proper $X_{\mathbf{k},\mathbf{k}}$) again we will use the exciton energies $E_{\mathbf{k}}$ as well as the strength $X_{\mathbf{k},\mathbf{k}}$ calculated for the finite homogeneous system. Thus, one may hope that the approximation Eq. (23) only affects the results for the spectra and the density of states in a rather weak way. In Sec. IV we will check the validity of the approximation by comparing this new application of the CPA directly to exact numerical simulations as well as to its traditional application, which uses periodic boundary conditions.

We end this section by noting that solving Eq. (21) for the self-energy usually requires numerical schemes. Our approach is to rewrite this equation in the form

$$\begin{aligned} \Sigma(\omega) &= \left[\int dx \mathcal{P}(x) \frac{x}{1 - (x - \Sigma(\omega))g_0(\omega)} \right] \\ &\times \left[\int dx \mathcal{P}(x) \frac{1}{1 - (x - \Sigma(\omega))g_0(\omega)} \right]^{-1}, \end{aligned} \quad (24)$$

which may be solved iteratively, using as starting value $\Sigma_0(\omega) = 0$, the value of $\Sigma(\omega)$ for the homogeneous system. The solution $\Sigma(\omega)$ to this equation in combination with the results described below Eq. (20) determines our CPA results for the spectra and density of states.

IV. NUMERICAL RESULTS FOR THE SPECTRA

In this paper, we restrict ourselves to the application of our formalism to the cylindrical aggregates occurring in the chlorosomes of the bacterium *Chloroflexus aurantiacus*.^{2,3,4,44} The application to the bilayer synthetic aggregates of carbocyanine dyes is discussed elsewhere.¹⁰ In terms of our stack of rings representation, the chlorosomal cylinders, consisting of tens of thousands of bacteriochlorophyll *c* molecules, have the following model parameters (see Refs. 19,44 and our discussion in Ref. 17): $N_2 = 6$, $h = 0.216$ nm, $\alpha = 189.6^\circ$, $\beta = 36.7^\circ$, and $\gamma = 20^\circ$. The radius is given by $R = 2.297$ nm, while the length may extend to hundreds of nanometers. Finally, we use an average single-molecule transition frequency ω_0 that agrees with a wavelength of 660 nm,^{45,46,47,48} while for the dipole squared of a single molecule we have used $\mu^2 \approx 20$ Debye². The latter value was obtained from the integrated extinction coefficient of monomeric solutions of BChl *c*,^{46,47,48} using the expression from Ref. 45.

Figure 2 presents the optical spectra for several cylinder lengths N_1 calculated using these model parameters and converted to a wavelength scale to facilitate the comparison to experiment.⁴⁹ All intermolecular dipole-dipole interactions were accounted for in these spectra. The solid lines represent the results obtained by numerical simulation, where we averaged over 1000 disorder realizations and used the rigorous smoothening technique proposed by Makhov *et al.*^{50,51} to reduce the noise in the spectra. For the disorder strength we used $\sigma = 600$ cm⁻¹, a value that was chosen such that the theoretical absorption linewidth agrees with the one observed experimentally at room temperature. Also plotted in Fig. 2 (dashed lines) are the results obtained using the CPA modified for open boundary conditions, as described in Sec. III. Finally, the dotted lines represent the spectra obtained within the traditional CPA, which assumes periodic boundary conditions in the n_1 direction (at finite N_1 values).

As is clear from Fig. 2, the modified CPA is in excellent agreement with the numerical simulations for all spectra and at all sizes. Both shape and position of the spectral features agree almost perfectly. We conclude that the finite-size effects in the spectra are captured in an excellent way by the approximation made in Eq. (23). These results justify the use of the CPA to model the spectra of wider cylinders,¹⁰ where the size of the one-exciton space becomes so large that the brute-force numerical simulation of the spectra becomes computationally too expensive.

To demonstrate that the proposed modification of the CPA is in fact essential to cover the finite-size effects, we have also applied the CPA in the traditional way, imposing periodic boundary conditions in the n_1 direction. In an attempt to still account for finite-size effects, we have however kept the length N_1 of the cylinder finite. We thus used Bloch waves for the longitudinal wave func-

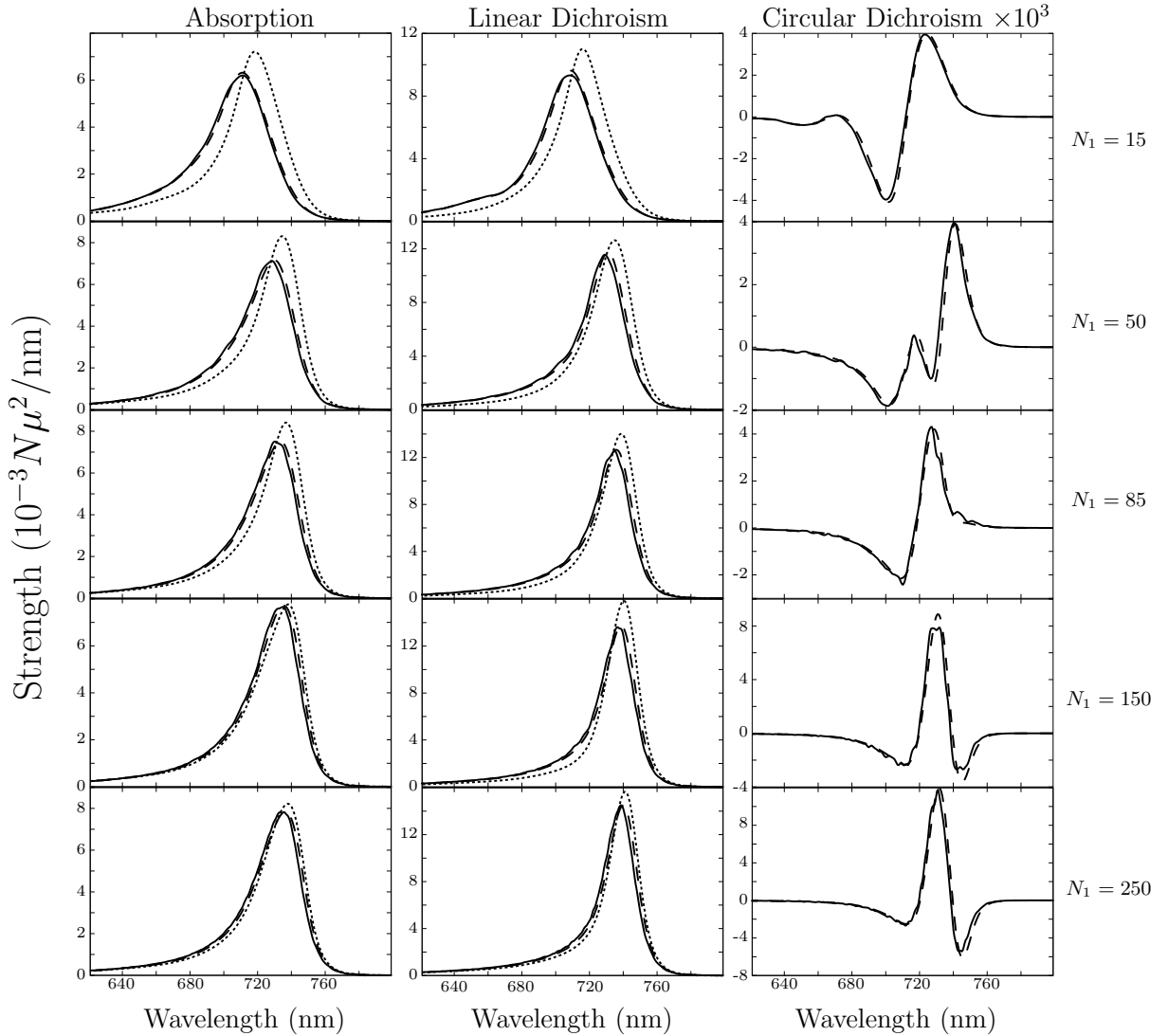


FIG. 2: Absorption, LD, and CD spectra calculated for cylindrical aggregates with the geometry of the rod elements in the chlorosomes of *Chloroflexus aurantiacus* (see text for details) and a disorder strength of $\sigma = 600 \text{ cm}^{-1}$. The solid lines are obtained by numerical simulations (average over 1000 disorder realizations) while the dashed lines are obtained using the modified CPA discussed in Sec. III. The dotted lines represent the usual implementation of the CPA, which starts from periodic boundary conditions. From top to bottom, the cylinder length is varied as follows: $N_1 = 15, 50, 85, 150$, and 250 .

tions $\varphi_{k_1}(n_1; k_2)$.¹⁷ The results for the absorption and LD spectra are shown as dotted curves in Fig. 2. For the CD spectrum, the use of periodic boundary conditions may be shown to be consistent only in the limit $N_1 \rightarrow \infty$,¹⁷ which is why dotted curves are absent in the CD panels. It is clear from Fig. 2 that the CPA with periodic boundary conditions yields spectra that differ notably from the exact ones, both in the position and shape of spectral features. The agreement is especially bad for short cylinders, where finite-size effects are most prominent. At all sizes considered (even for $N_1 = 250$) the modified CPA constitutes a better approximation than the one with periodic boundary conditions. We note that the spectra obtained by using periodic boundary conditions are always red-shifted relative to the exact and the modified-

CPA spectra. This results from the fact that for periodic boundary conditions every molecule interacts with other molecules that are at most half a cylinder length away, while using the correct open boundary conditions, the molecules near one edge of the cylinder (n_1 small) have much weaker interactions with the molecules at the other edge ($n_1 \approx N_1$). Thus, using periodic boundary conditions, one overestimates the effect of the interactions, which shifts the spectrum too far away from the monomer transition.

As final issue, we discuss the comparison between the exact spectra and the experimental ones. In our previous work¹⁷ we made this comparison neglecting the effects of disorder in the model. One may consider those previous results as one extreme case, where all spectral broadening

is assumed to arise from homogeneous broadening, while the current spectra constitute the other extreme situation, where the widths are assumed to purely result from inhomogeneity. Like in the homogeneous case reported in Ref. 17, we see that in particular the CD spectra exhibit a strong dependence on the length N_1 of the cylinder. This length dependence, specifically the change of the CD line shape around $N_1 = 100$, was an important point in our previous work, as it suggests that the strong variation in the reported CD spectra of chlorosomes^{52,53,54,55,56} results from the fact that different samples contain chlorosomes of different length. Apparently this conclusion survives the incorporation of disorder and the concomitant localization of the exciton states.

We stress that at the disorder value considered the typical exciton localization size in the region of the absorption band is several tens of molecules (Sec. V). Thus, one would expect the spectra to be size-saturated at cylinder lengths of at most several tens of rings. For the absorption and LD spectra, this indeed is the case, except that small shifts of the entire line shape still occur for longer cylinders as a result of the long-range dipole-dipole interactions. The slower size saturation for the CD spectrum results from two aspects. First, the presence of the intermolecular distances in the expression for the rotational strengths (cf. Eq. (11)) contribute to a prolonged size dependence. Second, being a difference spectrum, the CD spectrum is much more sensitive to the already mentioned small shifts in the exciton energies that result from the long-range interactions. The fact that for chlorosomes the length dependence of the CD spectrum survives the inclusion of disorder was also suggested by Prokhorenko et al.¹⁹ They based this conclusion on a study of the so-called CDM-matrix over a limited length interval, rather than a direct study of the spectrum.

While the spectra for the model with disorder follow the same general trends as those without disorder, the more detailed comparison to experiment is better for the case with disorder. First, in the presence of disorder the high-energy dip in the CD spectra for $N_1 > 100$ is seen to have a smaller amplitude than the low-energy dip, while this ratio is opposite for the homogeneous case.¹⁷ In experiment, the type of CD spectra with two negative dips indeed always have a smaller amplitude for the high-energy dip. The effect of disorder is to smear out the high-energy dip, giving it a smaller amplitude. Second, the presence of disorder gives the absorption and LD spectra a more pronounced high-energy tail than is obtained for the homogeneous model. Indeed, these tails, quite typical for disordered J aggregates, are observed in experiment.

To finish this section, we present in Fig. 3 the density of states for the disordered model (solid line, obtained from simulations) and the homogeneous one (dotted line), both for $N_1 = 250$. As above, the disorder was taken to be $\sigma = 600 \text{ cm}^{-1}$; the sticks in the density of states for the homogeneous case were convoluted with Lorentzian curves of FWHM = 20 cm^{-1} . The dis-

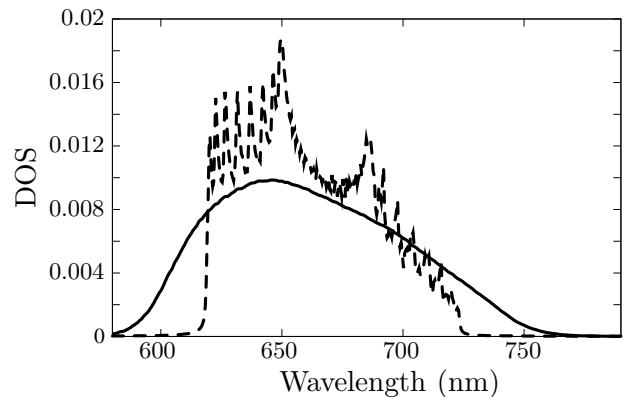


FIG. 3: Density of states for homogeneous (dashed line) and disordered (solid line) cylindrical aggregates of the chlorosome structure with a length of $N_1 = 250$ rings. In the former case, the excitons were homogeneously broadened by a Lorentzian of FWHM 20 cm^{-1} , while in the latter case a disorder strength of $\sigma = 600 \text{ cm}^{-1}$ was used. The disorder results were obtained from numerical simulations, averaging over 1000 realizations.

order clearly smears the discrete peaks still visible for the homogeneous case and leads to one broad feature that peaks somewhere in the middle of the exciton band. This is in marked contrast to the frequently studied one-dimensional aggregates, where the density of states, even in the presence of disorder, peaks at the band edges. So, even while the cylinder constitutes a strongly anisotropic system, its density of states deviates from a simple one-dimensional picture.

V. NUMERICAL RESULTS FOR THE LOCALIZATION CHARACTERISTICS

We now turn in more detail to the localization of the exciton wave functions. As a first step, we consider the participation ratio $\mathcal{L}^{-1}(\omega)$. In Fig. 4, we have plotted $9\mathcal{L}^{-1}(\omega)/4$ for chlorosomes within the homogeneous model (Fig. 4(a), $N_1 = 250$) and the disordered model (Fig. 4(b), $N_1 = 150, 200, 250$, and 300). In the homogeneous model we replaced the delta functions in Eq. (12) and the density of states by Lorentzians with a FWHM of 20 cm^{-1} , while in the disordered case (disorder strength $\sigma = 600 \text{ cm}^{-1}$, as in the previous section), we used the smoothening technique^{50,51} to reduce the noise in the simulations. The normalization factor $9/4$ was introduced to guarantee that for the homogeneous case we recover the total number of molecules N in the cylinder, see discussion below Eq. (12). This is clear from Fig. 4(a), where, indeed, inside the exciton band $9\mathcal{L}^{-1}(\omega)/4$ obtains an almost constant value of 1500 molecules, the total number of molecules in a cylinder of 250 rings.

In Fig. 4(b) we see that the disorder strength of 600 cm^{-1} leads to clear localization of the exciton states at all energies, even in the centre of the band, where the robustness against localization always is strongest. The

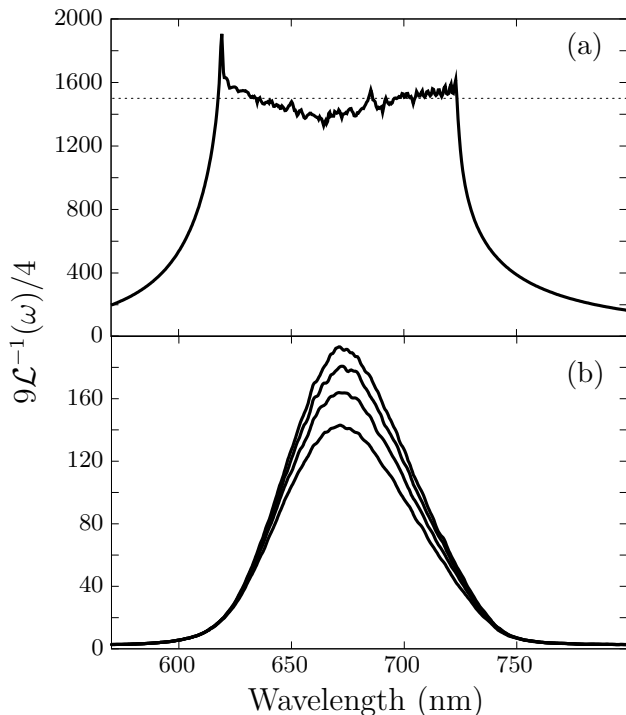


FIG. 4: (a) Energy dependent participation ratio for homogeneous cylindrical aggregates of the chlorosome structure with a length of $N_1 = 250$ rings. The dotted line indicates the total number of molecules (1500) in the cylinder. (b) As in panel (a), but now in the presence of diagonal disorder of strength $\sigma = 600 \text{ cm}^{-1}$ and considering four cylinder lengths. From top to bottom the curves correspond to $N_1 = 300, 250, 200$, and 150 , respectively.

fact that the band edge states are rather strongly localized is not surprising: the ratio of the disorder strength σ and the total exciton bandwidth is approximately 0.26. In the spectral region where the absorption band occurs (720 – 750 nm), the participation ratio yields a number of several tens of molecules over which the exciton states are delocalized. We emphasize that this number varies substantially (by a factor of 8) over the width of the absorption band. On the other hand, it is seen that in this energy region, the participation ratio hardly depends on the cylinder length anymore, which is in accordance with the fact that the exciton states are localized on a region of the cylinder that is much smaller than its total size. At the peak of the absorption spectrum (about 740 nm), the calculated participation ratio implies that the excitons are shared coherently by about 15 molecules (the autocorrelation function yields 11 molecules, see below). This value may be compared with the number of 7.4 – 7.6 obtained from measuring the bleaching ratio in absorption difference experiments.^{57,58} Given the large variation in the localization size over the absorption band, the arbitrariness and uncertainty present in any definition of a localization size, and the nonlinear nature of the absorption difference experiments, the agreement between our

simulations and these experimental data is good. Our localization size is considerably smaller than the 40 – 50 molecules obtained in the simulations of Prokhorenko et al.¹⁹ Still, for the same reasons as stressed above already, considerable room exists for deviations in the values reported from different model studies.

To obtain insight into the possible anisotropy of the localization properties, we also studied the autocorrelation function $\mathcal{C}(\mathbf{n}; \omega)$ defined in Eq. (13). We note that this anisotropy may also be studied by plotting individual wave functions, as we did in Fig. 10 of Ref. 18, but such plots have the drawback that they represent arbitrarily picked and *hopefully* typical states, while the correlation function gives statistical information. In Fig. 5 we present three-dimensional plots ((a)-(c)) as well as contour plots ((d)-(f)) of $\mathcal{C}(\mathbf{n}; \omega)$ for frequencies corresponding to wavelengths of, respectively, 700 nm, 740 nm, and 780 nm for a cylinder of length $N_1 = 250$ and a disorder strength of $\sigma = 600 \text{ cm}^{-1}$. To make these plots, the cylinder was cut along a line parallel to the z axis (the n_1 axis in the plots) and unwrapped.

Several observations can immediately be made from Fig. 5. First, with increasing energy the wave functions clearly get more extended, which is in agreement with Fig. 4(b). In fact, if we calculate $N_{del}^C(\omega)$ (defined at the end of Section II) from $\mathcal{C}(\mathbf{n}; \omega)$, we find for $N_1 = 250$ the values $N_{del}^C(700 \text{ nm}) = 147$, $N_{del}^C(740 \text{ nm}) = 11$, and $N_{del}^C(780 \text{ nm}) = 3$. These values are in reasonably good agreement with those obtained from the participation ratio: $9\mathcal{L}^{-1}(700 \text{ nm})/4 = 119$, $9\mathcal{L}^{-1}(740 \text{ nm})/4 = 15$, and $9\mathcal{L}^{-1}(780 \text{ nm})/4 = 2.9$. We also note that the values for $N_{del}^C(\omega)$ (and the plots for $\mathcal{C}(\mathbf{n}; \omega)$) at 740 and 780 nm do not depend on the cylinder length anymore at $N_1 = 250$. Second, as is most clearly visible in the contour plots, at the short length scale the wave functions exhibit a clear anisotropy along a direction that is neither given by $n_1 = \text{constant}$, nor by $n_2 = \text{constant}$, i.e., neither in the ring direction, nor in the direction of the helices drawn as dashed line in Fig. 1. In fact, the slanting direction of the contours relative to the vertical axis observed in Fig. 5 (which varies slightly with varying energy), closely resembles the slanting of the equal-phase lines of the wave functions in the $k_2 = \pm 1$ bands of the homogeneous cylinder discovered in Ref. 18. In the remainder of this section, we will explain this behavior, starting with a perturbative picture in which weak disorder mixes exciton states within and between the k_2 bands that exist for homogeneous cylinders.

In Ref. 18, we have shown that the optically dominant exciton states in the $k_2 = 0$ and $k_2 = \pm 1$ bands of the homogeneous cylinder are well approximated by analytical expressions of the form Eq. (20) with the ansatz

$$\varphi_{k_1}(n_1; k_2) = \sqrt{\frac{2}{N_1 + 1}} \sin\left(\frac{\pi k_1 n_1}{N_1 + 1}\right) e^{is(\theta_{k_2} + |k_2|\gamma)n_1}. \quad (25)$$

Here, k_1 is a positive integer, small compared to N_1 for the states of interest, $s = k_2/|k_2|$, γ is the helical angle of

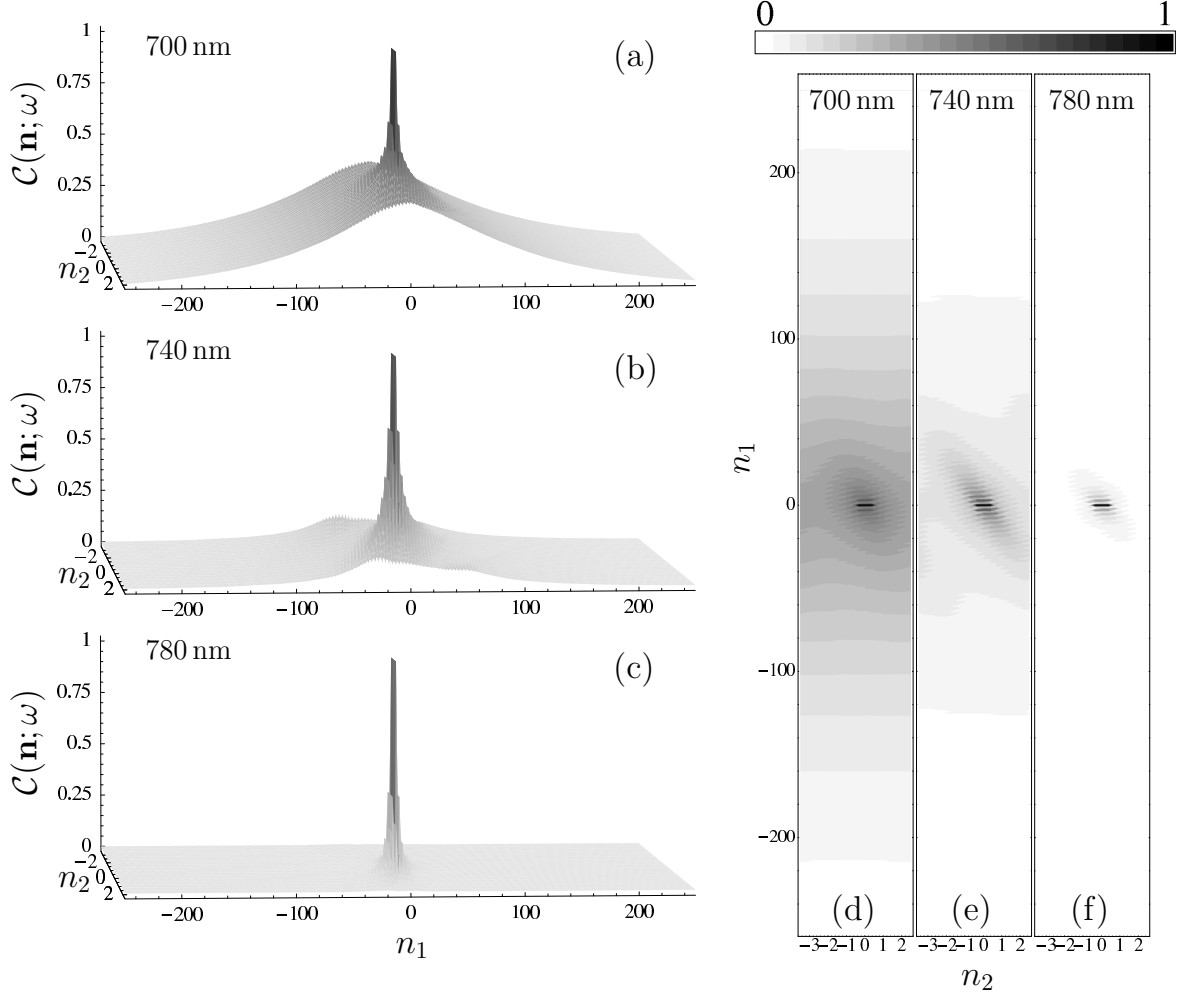


FIG. 5: Three-dimensional plots ((a)-(c)) and contour plots ((d)-(f)) of the autocorrelation function $\mathcal{C}(\mathbf{n}; \omega)$ [Eq. (13)] for cylindrical aggregates of the chlorosome structure with a length of $N_1 = 250$ rings and a disorder strength of $\sigma = 600 \text{ cm}^{-1}$ (averaged over 150 realizations) at three different energies, corresponding to 700 nm ((a) and (d)), 740 nm ((b) and (e)), and 780 nm ((c) and (f)). The cylinder surface is represented by cutting it along a line parallel to the z axis and unwrapping it. This cutting line is the n_1 axis in the plots; points with constant value of n_1 lie on the same ring of the cylinder. Due to the helical structure of chlorosomes, lines of constant n_2 make a finite angle with the n_1 direction (compare the dashed line in Fig. 1). The contour plots distinguish 25 equally large intervals for the value of $\mathcal{C}(\mathbf{n}; \omega)$, represented on a grayscale (see legend above the contour plots).

the cylinder (see Fig. 1), and θ_{k_2} is a phase angle that is used to optimize the quality of the ansatz for the complex effective one-dimensional Hamiltonian of the band with wave number k_2 .¹⁸ The ansatz Eq. (25) is exact if transfer interactions only occur between molecules on nearest-neighbor rings; in that case, the total angle $\theta_{k_2} + |k_2|\gamma$ is the phase of the effective nearest-ring interaction. Optimizing θ_{k_2} approximately accounts for mixing of the wave functions Eq. (25) by non-nearest-neighbor interactions.

The angle θ_{k_2} was found to be responsible for the slanting of equal-phase lines of the wave functions in the $k_2 = \pm 1$ band of the homogeneous cylinder (chirality of the wave functions) relative to the vertical axis, which seems essential to understand the behavior of $\mathcal{C}(\mathbf{n}; \omega)$ observed in Fig. 5(d)-(f). We therefore reconsider the ansatz solutions Eq. (25), with a special focus on θ_{k_2} and extending the treatment to the bottom regions of all k_2 bands.

The $k_2 = 0$ band. The Hamiltonian for the $k_2 = 0$

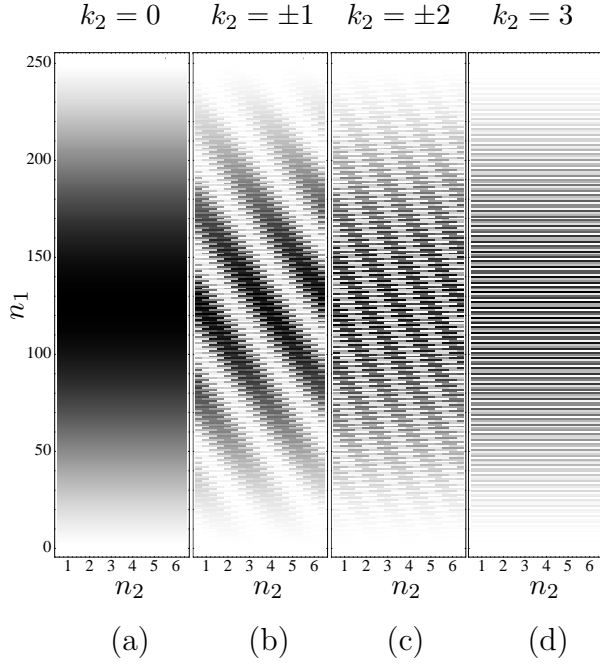


FIG. 6: Gray-scale density plots of the squared amplitudes (darker represents a higher amplitude) of the lowest states in the six exciton bands of homogeneous cylindrical aggregates of the chlorosome structure with a length of $N_1 = 250$ rings: $k_2 = 0$ (a), $k_2 = \pm 1$ (b), $k_2 = \pm 2$ (c), and $k_2 = 3$ (d). Plots are given on the unwrapped cylinder surface. The wave functions were obtained from exact diagonalization of the corresponding homogeneous Hamiltonians and are well described by Eq. (20), with the ansatz Eq. (25) (see text for details). Relative to the average molecular transition energy ω_0 , the lowest states have the energies -1288.73 cm^{-1} (a), -1291.92 cm^{-1} (b), -1244.97 cm^{-1} (c), and -1166.09 cm^{-1} (d).

band is real, implying that also the wave functions can be chosen real. Hence, we have $\theta_0 = 0$. It was shown in Ref. 18 that the bottom state of this band (the $k_1 = 1$ state, which carries 81% of the oscillator strength in this band) is well described by the ansatz. For this band, the wave function has equal amplitude on all molecules of a certain ring, while the quantum number k_1 gives the number of maxima along the z axis of the cylinder. This is illustrated in Fig. 6(a), where we plotted the amplitude squared of the exact wave function (obtained by numerical diagonalization) of the lowest state in the $k_2 = 0$ band of the homogeneous cylinder.

The $k_2 = \pm 1$ bands. The effective Hamiltonian for these two degenerate bands is essentially complex and the phase factor in Eq. (25) is needed. In Ref. 18 we have shown that the superradiant states (three in each band) all occur near $k_1 = k^* = \text{nint}[|\theta_1|(N_1 + 1)/\pi]$ (nint denoting the nearest integer function), which is a finite energy above the bottom of the $k_1 = \pm 1$ bands. Excellent agreement was found between the ansatz wave functions and those for the superradiant states of the homogeneous cylinder obtained by numerical diagonalization for the

optimized value of $\theta_{\pm 1} = 4.3^\circ$.¹⁸ Presently, we are not only interested in the superradiant states, but even more so in the states near the bottom of the $k_2 = \pm 1$ bands (k_1 in the order of unity), because these states are closest to the bottom of the $k_2 = 0$ band and should be expected to mix with those states in the presence of (weak) disorder. We may apply the same approach as followed in Ref. 18 for the superradiant states to the states near the band bottom. Thus, we fix $\theta_{\pm 1}$ such that the mixing between the bottom states in the $k_2 = \pm 1$ bands resulting from the long-range interactions does not diverge. This eventually yields $\theta'_{\pm 1} = 3.8^\circ$ (for $N_1 = 250$), which only slightly differs from the phase angle in the superradiant region.

If we plot the amplitude squared of the exciton wave function on the unwrapped cylinder, a state of the form Eq. (20) with Eq. (25) gives lines of equal intensity that are dictated by lines of equal phase $s(\theta_{k_2} + |k_2|\gamma)n_1 + 2\pi k_2 n_2 / N_2$. The angle χ of these lines with the z axis is easily derived to obey

$$\tan \chi = -\frac{\theta_{k_2} R}{|k_2| h}. \quad (26)$$

This implies that the wave function rotates around the cylinder over a number rings given by

$$n_1^* = 2\pi |k_2| / \theta_{k_2}. \quad (27)$$

From this we find that in $k_2 = \pm 1$ bands $n_1^* \approx 84$ for the wave functions of the superradiant states and $n_1^* \approx 95$ for the bottom states. In Fig. 6(b) we show the amplitude squared for the bottom state of the $k_2 = 1$ band obtained by numerical diagonalization. Of course, on every ring we find a modulation with two maxima, as is appropriate for this band. More importantly, we find good agreement between the value of n_1^* that may be obtained from this plot and the above estimate obtained from the ansatz wave function.

The $k_2 = \pm 2$ bands. These bands, which contain no oscillator strength in the homogeneous limit, were not considered in Ref. 18. They may be treated in a way similar to the $k_2 = \pm 1$ bands. If we focus on optimizing the ansatz at the bottom of the bands, we find $\theta_{\pm 2} = 6.6^\circ$ for $N_1 = 250$ and that for this value the ansatz Eq. (25) for $k_1 = 1$ indeed gives a good description of the numerically obtained lowest state. From Eq. (27) and $\theta_{\pm 2} = 6.6^\circ$ a value of $n_1^* \approx 109$ can be estimated, which is seen to be in good agreement with the exact wave function plotted in Fig. 6(c). Of course, the states in the $k_2 = \pm 2$ bands exhibit a modulation of squared amplitudes inside each ring with four maxima.

The $k_2 = 3$ band. This band, too, has no oscillator strength. Like the $k_2 = 0$ band, the $k_2 = 3$ band is non-degenerate and is governed by a real Hamiltonian. Thus, $\theta_3 + 3\gamma = 0$ and, like for the $k_2 = 0$ case, no optimization condition for θ_3 has to be solved. Figure 6(d) gives the amplitude squared of the numerically obtained lowest state in this band, which exhibits no modulation inside

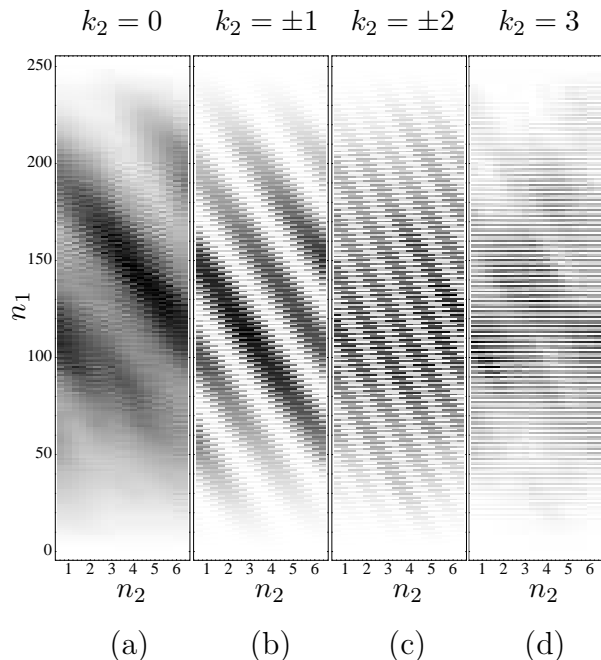


FIG. 7: As in Fig. 6, but now including diagonal disorder of a strength $\sigma = 20 \text{ cm}^{-1}$. The weakness of the disorder allows for an identification to the \mathbf{k} states of the homogeneous aggregate in Fig. 6. The energies of the plotted states are -1288.96 cm^{-1} (a), -1292.67 cm^{-1} (b), -1245.97 cm^{-1} (c), and -1167.55 cm^{-1} (d).

rings (the Bloch factor is $(-1)^{n_2}$ which gives unity upon taking the square). One does observe a vertical modulation with a high periodicity, which is due to the fact that for this band the lowest state is not the $k_1 = 1$ state, but rather a state that corresponds to a high value of k_1 . This is due to the fact that for this band the effective Hamiltonian has dominant positive instead of negative interactions.

The important conclusion of the above analysis is that the bottom states in the $k_2 = 0$ and $k_2 = 3$ bands exhibit no chiral behavior (no equal-intensity lines slanted relative to the z axis), while the bottom states of the $k_2 = \pm 1$ and the $k_2 = \pm 2$ bands do show a chirality which, moreover, is very similar in magnitude as estimated by the number n_1^* . If we now allow for weak disorder, mixing of the \mathbf{k} states within and between bands will occur. Focusing on the bottom region of the density of states, we thus find that the wave functions in the homogeneous $k_2 = 0$ and $k_2 = 3$ bands will (perturbatively) acquire a slanted contribution as well. In view of the fact that the slant angle varies little inside as well as between the $k_2 = \pm 1$ and $k_2 = \pm 2$ bands, we thus expect a similar slanting for all low-energy states at weak disorder. This is clearly confirmed by Fig. 7, where we presented the bottom states of the $k_2 = 0, 1, 2$, and 3 bands weakly perturbed by the presence of a very small disorder strength of $\sigma = 20 \text{ cm}^{-1}$. If we further increase the disorder strength, the mixing will become nonpertur-

bative and will also involve higher-lying states, described by different χ values and a different number of nodes in the vertical direction. These are the ingredients for the localization visible in Fig. 5; however, the slanting of the autocorrelation function still clearly reflects the fact that locally the wave functions have a chirality that derives from the homogeneous states. The reason is that this chirality is mainly driven by the dominant transfer interactions, which occur over a few rings.

VI. CONCLUSIONS

In this paper we have theoretically investigated the effects of disorder on the linear optical properties and the localization behavior of the exciton states of cylindrical molecular aggregates. As specific example, we have used the structure for the cylindrical aggregates found in the light harvesting systems (chlorosomes) of green bacteria. We have calculated the absorption, LD, and CD spectra for various cylinder lengths in the presence of Gaussian diagonal disorder, using both numerical simulations and the CPA. To this end, we modified the usual implementation of the CPA to account for finite-size effects (open boundary conditions). By comparison to the simulation results, we have shown that this new implementation yields an excellent approximation, in fact significantly better than the usual CPA, which starts from periodic boundary conditions. We have shown that for the chlorosomes the inclusion of disorder improves the comparison to experiment in several respects. Most importantly, however, the inclusion of disorder does not affect the main conclusion of Ref. 17 that the CD spectrum has a strong size dependence up to cylinders of hundreds of rings long. We demonstrated and discussed that this effect occurs in spite of the fact that the exciton localization size is far smaller than the cylinder size.

The localization behavior of the excitons was studied by examining two quantities: the participation ratio and an autocorrelation function of the exciton wave functions. While the former only yields an approximate measure for the number of molecules participating in the excitation, the latter gives additional information about the direction of localization on the cylinder. In the case of chlorosomes, we found that the excitons that dominate the optical properties (the ones near the band bottom) have a strongly anisotropic localization behavior, being extended mainly along helices, whose direction is dictated by the interplay of the various intermolecular excitation transfer interactions in the cylinder. As we have demonstrated, this chiral behavior finds its roots in the chirality of the fully extended exciton states for the homogeneous cylinder. Both the participation ratio and the autocorrelation function show that, starting from the bottom of the exciton band, the exciton states become more extended with increasing energy (both quantities give comparable values for the energy dependent localization size). Also the chirality of the wave functions is energy depen-

dent, but this effect is small. It is of interest to speculate whether the chiral nature of the wave functions could be detected in terms of a rotating polarization of the light emitted by an exciton while propagating. This would require single-aggregate experiments with high spatial resolution and a time-resolved detection.^{59,60}

Acknowledgment

This work is part of the research program of the Stichting voor Fundamenteel Onderzoek der Materie (FOM),

which is financially supported by the Nederlandse Organisatie voor Wetenschappelijk Onderzoek (NWO).

- ¹ L. A. Staehelin, J. R. Golecki, and G. Drews, *Biochim. Biophys. Acta* **589**, 30 (1980).
- ² A. R. Holzwarth and K. Schaffner, *Photosynth. Res.* **41**, 225 (1994).
- ³ T. S. Balaban, A. R. Holzwarth, and K. Schaffner, *J. Mol. Struct.* **349**, 183 (1995).
- ⁴ B. J. van Rossum, G. J. Boender, F. M. Mulder, J. Raap, T. S. Balaban, A. R. Holzwarth, K. Schaffner, S. Prytulla, H. Oschkinat, and H. J. M. de Groot, *Spectrochim. Acta, Part A* **54**, 1167 (1998).
- ⁵ T. Mizoguchi, S. Sakamoto, Y. Koyama, K. Ogura, and F. Inagaki, *Photochem. Photobiol.* **67**, 239 (1998).
- ⁶ B. J. van Rossum, D. B. Steensgaard, F. M. Mulder, G. J. Boender, K. Schaffner, A. R. Holzwarth, and H. J. M. de Groot, *Biochemistry* **40**, 1587 (2001).
- ⁷ S. Kirstein, H. von Berlepsch, C. Böttcher, C. Burger, A. Ouart, G. Reck, and S. Dähne, *ChemPhysChem* **1**, 146 (2000).
- ⁸ H. von Berlepsch, C. Böttcher, A. Ouart, C. Burger, S. Dähne, and S. Kirstein, *J. Phys. Chem. B* **104**, 5255 (2000).
- ⁹ H. von Berlepsch, S. Kirstein, R. Hania, C. Didraga, A. Pugžlys, and C. Böttcher, *J. Phys. Chem. B* **107**, 14176 (2003).
- ¹⁰ C. Didraga, P. R. Hania, A. Pugžlys, H. von Berlepsch, K. Duppen, and J. Knoester, in press.
- ¹¹ J. P. Hill, W. Jin, A. Kosaka, T. Fukushima, H. Ichihara, T. Shinomura, K. Ito, T. Hashizume, N. Ishii, and T. Aida, *Science* **304**, 1481 (2004).
- ¹² S. C. M. Gandini, E. L. Gelamo, R. Itri, and M. Tabak, *Biophys. J.* **85**, 1259 (2003).
- ¹³ R. Rotomskis, R. Augulis, V. Snitka, R. Valiokas, and B. Liedberg, *J. Phys. Chem. B* **108**, 2833 (2004).
- ¹⁴ D. Hu, J. Hu, B. Bagchi, P. R. Rossky, and P. F. Barbara, *Nature* **405**, 1030 (2000).
- ¹⁵ M. Bednarz and J. Knoester, *J. Phys. Chem. B* **105**, 12913 (2001).
- ¹⁶ C. Spitz, J. Knoester, A. Ouart, and S. Dähne, *Chem. Phys.* **275**, 271 (2002).
- ¹⁷ C. Didraga, J. A. Klugkist, and J. Knoester, *J. Phys. Chem. B* **106**, 11474 (2002).
- ¹⁸ C. Didraga and J. Knoester, *J. Chem. Phys.* **121**, 946 (2004).
- ¹⁹ V. I. Prokhorenko, D. B. Steensgaard, and A. R. Holzwarth, *Biophys. J.* **85**, 3173 (2003).
- ²⁰ M. Schreiber and Y. Toyozawa, *J. Phys. Soc. Jpn.* **51**, 1528 (1981).
- ²¹ M. Schreiber and Y. Toyozawa, *J. Phys. Soc. Jpn.* **51**, 1537 (1981).
- ²² H. Fidder, J. Knoester, and D. A. Wiersma, *J. Chem. Phys.* **95**, 7880 (1991).
- ²³ A. V. Malyshev and V. A. Malyshev, *Phys. Rev. B* **63**, 195111 (2001).
- ²⁴ M. Chachisvilis, O. Kühn, T. Pullerits, and V. Sundström, *J. Phys. Chem. B* **101**, 7275 (1997).
- ²⁵ T. Meier, V. Chernyak, and S. Mukamel, *J. Phys. Chem. B* **101**, 7332 (1997).
- ²⁶ O. Kühn and V. Sundström, *J. Chem. Phys.* **107**, 4154 (1997).
- ²⁷ V. Agranovich, *Zh. Exp. Teor. Fiz.* **37**, 430 (1959), engl. transl.: *Sov. Phys. JETP* **37**, 307 (1960).
- ²⁸ V. Agranovich, *Fiz. Tverd. Tela* **3**, 811 (1961), engl. transl.: *Sov. Phys. Solid State* **3**, 592 (1961).
- ²⁹ A. S. Davydov, *Theory of Molecular Excitons* (Plenum, New York, 1971).
- ³⁰ V. M. Agranovich and M. D. Galanin, in *Electronic Excitation Energy Transfer in Condensed Matter*, edited by V. M. Agranovich and A. A. Maradudin (North-Holland, Amsterdam, 1982).
- ³¹ P. Soven, *Phys. Rev.* **156**, 809 (1967).
- ³² D. W. Taylor, *Phys. Rev.* **156**, 1017 (1967).
- ³³ J. Hoshen and J. Jortner, *J. Chem. Phys.* **56**, 5550 (1972).
- ³⁴ H. Port, H. Nissler, and R. Silbey, *J. Chem. Phys.* **87**, 1994 (1987).
- ³⁵ A. Boukahil and D. L. Huber, *J. Lumin.* **45**, 13 (1990).
- ³⁶ A. Boukahil and D. L. Huber, *J. Lumin.* **48-49**, 255 (1991).
- ³⁷ L. D. Bakalis, I. Rubtsov, and J. Knoester, *J. Chem. Phys.* **117**, 5393 (2002).
- ³⁸ P. W. Anderson, *Phys. Rev.* **109**, 1492 (1958).
- ³⁹ D. J. Thouless, *Phys. Rep.* **13**, 93 (1974).
- ⁴⁰ The states $\mathbf{k} = (0, 0)$ and $(N_1/2, N_2/2)$ have a participation ratio $1/N$, while a participation ratio of $3/2N$ is obtained for the states $(0, k_2)$, $(k_1, 0)$, $(N_1/2, k_2)$, and $(k_1, N_2/2)$, with $k_i \notin \{0, N_i/2\}$; Of course the states $N_i/2$ exist only when N_i is even.
- ⁴¹ O. Kühn and V. Sundström, *J. Chem. Phys.* **107**, 4154 (1997).
- ⁴² G. Rickayzen, *Green's Functions in Condensed Matter* (Academic, New York, 1980).
- ⁴³ E. N. Economou, *Green's Functions in Quantum Physics* (Springer Verlag, Berlin, 1983).
- ⁴⁴ V. I. Prokhorenko, D. B. Steensgaard, and A. R. Holzwarth,

- Biophys. J. **79**, 2105 (2000).
- ⁴⁵ C. Houssier and K. Sauer, J. Amer. Chem. Soc. **92**, 779 (1970).
- ⁴⁶ N. U. Frigaard, K. L. Larsen, and R. P. Cox, FEMS Microbiol. Ecology **20**, 69 (1996).
- ⁴⁷ A. Dudkowiak, C. Francke, J. Amesz, A. Planner, I. Hanyż, and D. Frąckowiak, Spectrochim. Acta A **52**, 251 (1996).
- ⁴⁸ M. Umetsu, Z. Y. Wang, M. Kobayashi, and T. Nozawa, Biochim. Biophys. Acta **1410**, 19 (1999).
- ⁴⁹ We use $S(\lambda) = S(\omega)d\omega/d\lambda$.
- ⁵⁰ D. V. Makhov, V. V. Egorov, A. A. Bagaturyants, and M. V. Alfimov, Chem. Phys. Lett. **246**, 371 (1995).
- ⁵¹ D. V. Makhov, V. V. Egorov, A. A. Bagaturyants, and M. V. Alfimov, J. Chem. Phys. **110**, 3196 (1999).
- ⁵² K. Griebenow, A. R. Holzwarth, F. van Mourik, and R. van Grondelle, Biochim. Biophys. Acta **1058**, 194 (1991).
- ⁵³ R. P. Lehmann, R. A. Brunisholz, and H. Zuber, Photosynth. Res. **41**, 165 (1994).
- ⁵⁴ Z. Y. Wang, G. Marx, M. Umetsu, M. Kobayashi, M. Mimuro, and T. Nozawa, Biochim. Biophys. Acta **1232**, 187 (1995).
- ⁵⁵ R. Frese, U. Oberheide, I. van Stokkum, R. van Grondelle, M. Foidl, J. Oelze, and H. van Amerongen, Photosynth. Res. **54**, 115 (1997).
- ⁵⁶ D. B. Steensgaard, C. A. van Walree, H. Permentier, L. Bañeras, C. M. Borrego, J. Garcia-Gil, T. J. Aartsma, J. Amesz, and A. R. Holzwarth, Biochim. Biophys. Acta **1457**, 71 (2000).
- ⁵⁷ S. Savikhin, D. Buck, W. S. Struve, R. E. Blankenship, A. S. Taisova, V. I. Novoderezhkin, and Z. G. Fetisova, FEBS Lett. **430**, 323 (1998).
- ⁵⁸ A. Yakovlev, V. I. Novoderezhkin, A. Taisova, and Z. Fetisova, Photosynth. Res. **71**, 19 (2002).
- ⁵⁹ C. Hofmann, M. Ketelaars, M. Matsushita, H. Michel, T. J. Aartsma, and J. Köhler, Phys. Rev. Lett. **90**, 13004 (2003).
- ⁶⁰ J. Yu, D. Hu, and P. F. Barbara, Science **289**, 1327 (2000).